Magnetism of $(LaCoO_3)_n+(LaTiO_3)_n$ superlattices ($n = 1, 2$)

Alex Taekyung Lee and Sohrab Ismail-Beigi

Department of Applied Physics, Yale University, New Haven, Connecticut 06520, USA

$LaCoO_3$ provides a poignant example of a transition metal oxide where the cobalt cations display multiple spin states and spin transitions and which continues to garner substantial attention. In this work, we describe first principles studies, based on DFT+U theory, of superlattices containing $LaCoO_3$, specifically $(LaCoO_3)_n+(LaTiO_3)_n$ for $n = 1, 2$. The superlattices show strong electron transfer from Ti to Co resulting in Co^{2+}, significant structural distortions and a robust orbital polarization of the Co^{2+}. We predict high-spin Co^{2+} and a checkerboard (G-type) antiferromagnetic ground state. We provide a detailed analysis of the magnetic interactions and phases in the superlattices. We predict that ferromagnetic order on the Co^{2+} can be stabilized by hole doping (e.g., replacing La by Sr), which is rather unusual for Co^{2+} cations.

I. INTRODUCTION

Transition metal perovskite oxides (with chemical formula ABO_3, where A is a rare earth and B is a transition metal) display fascinating physical properties, such as high-temperature superconductivity in the cuprates or colossal magnetoresistance in the manganites [1,2]. The electronic and structural properties of perovskites and intertwined and lead to complex behaviors due to the interplay of charge, magnetic, structural, and orbital degrees of freedom [3]. Creating heterostructures of transition metal perovskites enlarges the playground for manipulation of the local structure, charge state and electronic properties of these materials. In this work, we focus on the electronic states of cobalt-containing perovskites.

Bulk $LaCoO_3$ has attracted much attention because of the complex electronic and magnetic structure of the Co^{3+} cations it contains. $LaCoO_3$ is a nonmagnetic insulator at the lowest temperatures [4,5] when the Co^{3+} adopt a low-spin (LS) state (t_{2g}^6, $S = 0$). It becomes a paramagnetic insulator for temperatures 100 K $< T <$ 500 K and then becomes metallic above 500 K. However, the spin state of Co in the thermally excited material is still under debate. The magnetic transition near 100 K is considered as a transition from LS to high-spin (HS) ($t_{2g}^4 e_g^2$, $S = 2$) [6,7] or to intermediate spin (IS) ($t_{2g}^5 e_g^1$, $S = 1$) states [5,8–11], while IS and HS are mixed as temperature increases [10,11].

First principles density functional theory (DFT) calculations based on DFT+U theory [12] for $LaCoO_3$ confirm that the LS state is the ground state [13–15], while the IS state is more stable than HS [13]. On the other hand, several theoretical studies suggested that the excited state at 100 K $< T <$ 500 K can be a mixture of HS and LS, which we denote as HS/LS below. Using the experimental crystal structures as a function of temperature, GGA+U calculations suggested that HS/LS is stabilized for the structures above 200 K [15]. Unrestricted Hartree-Fock calculations also proposed that the nonmagnetic to paramagnetic transition is due to the LS state to LS/HS state [16], and effective Hamiltonian calculations

suggested a similar scenario [17,18]. Recent DFT+dynamical mean-field theory calculations showed that $LaCoO_3$ has large charge fluctuations: these calculations show that it is not possible to explain the spin state with a single multiplet at any temperature, although they find that at the onset of the spin-spin transition HS multiplets are excited with the IS multiplets being excited later around the onset of the metal-insulator transition [19].

On the other hand, the electronic and magnetic structures of Co^{2+} in bulk CoO does not show such complexity or ambiguity. At low temperatures, CoO is an insulator with energy gap $E_g = 2.4$ eV [20]. The Co^{2+} cations have a HS state ($t_{2g}^5 e_g^2$ with $S = 3/2$), and antiferromagnetically order at $T_N = 289$ K with a magnetic ordering wave vector of $\boldsymbol{q}_{fcc} = (\frac{1}{2}, \frac{1}{2}, \frac{1}{2})$ [21,22]. Unlike $LaCoO_3$, Co^{2+} in CoO does not show LS or IS states nor a spin-state transition.

An intriguing set of questions arise as to what happens if the Co^{2+} cations are realized in a perovskite heterostructure containing $LaCoO_3$. Is the difference between the electronic behavior of $LaCoO_3$ and CoO only due to charge state of the Co cations? To what extent can the Co electronic properties be controlled or manipulated by changing the local lattice structure surrounding the Co cation? And how can one make strong modifications to the local structure? One way to control the charge state of transition metal cations and the local lattice structure is via heterostructuring. For example, charge transfer can be triggered from Ti to Ni in $LaNiO_3+LaTiO_3$ superlattices [23,24], which results in a Ni^{2+} charge state with large e_g orbital polarization, which is in strong contrast to the orbitally unpolarized Ni^{3+} in bulk $LaNiO_3$. Recent work on $LaCoO_3+LaTiO_3$ superlattices also shows charge transfer and robust orbital polarization [25].

In this work, we study the electronic and magnetic properties of Co in $(LaTiO_3)_1+(LaCoO_3)_1$ and $(LaTiO_3)_2+(LaCoO_3)_2$ superlattices using DFT+U theory. We explore carefully the effect of the Hubbard U parameter, account for the effects of different exchange-correlation approximations, and examine the effect of strain from the

substrate, as well as the effects of doping. We explain the origin of the magnetic stabilities for different spin states and magnetic orderings by using a simple band interaction picture. Interestingly, from the analysis of the magnetic stabilities, we are able to show that ferromagnetic spin order on for the Co^{2+} cations can be stabilized in the $(LaTiO_3)_1+(LaCoO_3)_1$ superlattice by hole doping which is an unexpected and unique finding for Co^{2+} as detailed below (Summary and Outlook section). We note that recent experiments [25] have studied only the $(LaTiO_3)_2+(LaCoO_3)_2$ superlattice, so our results for the $(LaTiO_3)_1+(LaCoO_3)_1$ superlattice present exciting predictions for experiments.

This paper is organized as follows. Section II describes our computational approach. Section III describes the key predicted superlattice properties: structure, electron transfer, Co spin states, and magnetic properties as a function of strain and doping. Section IV A is devoted to analyzing and understanding computed properties: energetics of HS and LS states as a function of U_{Co}, the origin of the U_{Co} dependences, stabilities of various magnetic orderings as a function of U_{Co}, a simple band interaction model for understanding the results, further strain effects, the effects of different exchange-correlation approximations, the cause of the stabilization of ferromagnetism in hole-doped $(LaCoO_3)_1+(LaTiO_3)_1$ super-lattices. In Sec. IV B we apply the above analysis of electronic and magnetic properties to the $(LaCoO_3)_2+(LaTiO_3)_2$ superlattice and describe the importance of out-of-plane Co–Co magnetic interaction. We then summarize the work and provide an outlook.

II. COMPUTATIONAL DETAILS

We use density functional theory (DFT) with the projector augmented wave (PAW) method [26] and the revised version of the generalized gradient approximation (GGA) proposed by Perdew *et al.* (PBEsol) [27] as implemented in the VASP software [28]. We also have done selective tests using the local density approximation (LDA) [29,30]. In all cases, the spin-dependent version of the exchange correlation functional is employed. A plane wave basis with a kinetic energy cutoff of 500 eV is used. We use Γ-centered **k**-point meshes of size $9 \times 9 \times 7$ and $9 \times 9 \times 5$ for $(LaCoO_3)_1+(LaTiO_3)_1$ and $(LaCoO_3)_2+(LaTiO_3)_2$, respectively. The sizes of the supercells for $(LaCoO_3)_1+(LaTiO_3)_1$ and $(LaCoO_3)_2+(LaTiO_3)_2$ are 20 and 40 atoms, respectively, corresponding to $\sqrt{2} \times \sqrt{2}$ [i.e., $c(2 \times 2)$] in-plane unit cells. These unit cells have two Co atoms in each CoO_2 plane, so that the $(LaCoO_3)_1+(LaTiO_3)_1$ and $(LaCoO_3)_2+(LaTiO_3)_2$ each have two and four Co atoms in their unit cells, respectively. Atomic positions within the unit cells were relaxed until the residual forces were less than 0.01 eV/Å in all axial directions, and the stress is less than 0.5 kB along the z axis.

The GGA+U scheme within the rotationally invariant formalism together with the fully localized limit double-counting formula [12] is used to study the effect of electron interactions within the $3d$ orbital manifolds. The electronic and structural properties critically depend on U_{Co}, and therefore we carefully explore a range of values. We also explore how the results depend on U_{Ti}, which plays a secondary role in the physics of these materials. We do not employ an on-site exchange

interaction J for any species, as the exchange interaction is already accounted for within the spin-dependent DFT exchange-correlation potential [31,32]. We used maximally localized Wannier functions (MWLFs) as implemented by the Wannier90 software [33] to obtain a localized tight-binding representation describing Co $3d$-derived bands. Finally, we point the reader to the Appendix for our results on the U dependence of the properties of bulk $LaCoO_3$, CoO, and $LaTiO_3$ which help us find proper ranges and reasonable values for the U parameters.

III. KEY RESULTS

A. $(LaCoO_3)_1+(LaTiO_3)_1$ superlattice

In this subsection, we discuss our key findings for the atomic, electronic, and magnetic properties of $(LaCoO_3)_1+(LaTiO_3)_1$ superlattices.

1. Structure

We begin with the structure of the $LaCoO_3+LaTiO_3$ (LCO+LTO) superlattices. Our supercell of $(LTO)_1+(LCO)_1$ has a $c(2 \times 2)$ in-plane unit cell and therefore two distinct Co atoms. In addition to the relaxation of the shape of the local oxygen octahedra, resulting in Jahn-Teller-like distortions, tilting of oxygen octahedra is also important in determining the electronic structure of transition metal oxides. Unlike bulk oxides, the tilt pattern of the superlattice is harder to observe experimentally (due to thinness of the samples) and is not known *a priori*, so we consider several tilt patterns and choose the most stable one. Since bulk LCO has the $R\bar{3}c$ crystal structure with $a^-a^-a^-$ octahedral tilts and bulk $LaTiO_3$ has the *Pbnm* structure with $a^-a^-b^+$ tilts, we examine three cases: $a^0a^0a^0$, $a^-a^-a^-$ and $a^-a^-b^+$. We find that $a^-a^-b^+$ is always the most stable, so we examine only this tilt pattern below unless otherwise specified (see Fig. 1).

The structures are relaxed along the c axis, which is normal to the interface, while in-plane lattice parameters a and b are fixed and set equal $a = b$ to simulate epitaxial strain from a substrate. Three in-plane lattice parameter values are used below: 3.663 Å, 3.784 Å, and 3.905 Å. The two values 3.784 Å and 3.905 Å are the experimental lattice parameters of $LaAlO_3$ (LAO) and $SrTiO_3$ (STO) substrates, respectively. To study the effect of the compressive strain on LCO, we use 3.663 Å, which is smaller than the LCO lattice. We note that the optimized lattice parameter of bulk LCO within our GGA+U calculations (with $U_{Co} = 3$ eV) is 3.805 Å, which is close to the LAO lattice constant.

2. Electron transfer from Ti to Co

Next we discuss the charge states of transition metals and the electron transfer. Given the difference in electronegativity between Ti and Co [34,35], electron transfer is expected from Ti $3d$ to Co $3d$ across the interface. Projected densities of states (see Fig. 2) within GGA+U show that the Ti d bands are unoccupied, which corresponds to Ti^{4+}, and describe the conduction band minimum. On the other hand, Co has 2+ charge state with d^7 electrons, indicating full charge transfer (formal charge).
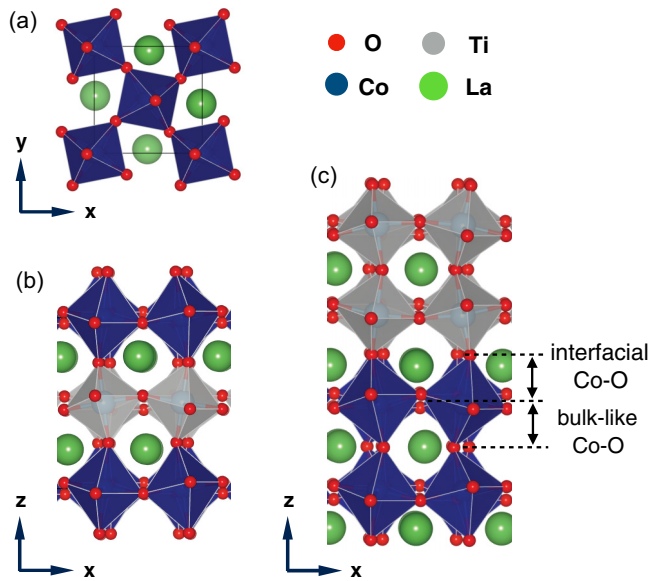
FIG. 1. Atomic-scale structures of $(LaCoO_3)_1+(LaTiO_3)_1$ and $(LaCoO_3)_2+(LaTiO_3)_2$ superlattices. (a) Top view and (b) side view of the $(LaCoO_3)_1+(LaTiO_3)_1$ superlattice. (c) Side view of the $(LaCoO_3)_2+(LaTiO_3)_2$ superlatttice.

In order to further examine the nature of the charge transfer, we computed the mean energy of the $3d$ orbitals of Ti and Co (by using the projected density of states as weight) to learn about the electronic potential landscape across the interface [36]. For $(LCO_3)_1+(LTO_3)_1$ and $(LCO_3)_2+(LTO_3)_2$, the Ti $3d$ atomic orbitals are higher than the Co $3d$ by 5.2 and 1.9 eV, respectively.

Due to the charge transfer, we have Ti^{4+} and Co^{2+}, and we expect local electric fields pointing from the $TiO2$ layers to the CoO_2 layers. This can be confirmed by looking at the positions of the positively charged La^{3+} cations and negatively charged apical oxygen anions (O^{2-}): the displacements are visible to the eye in Fig. 1. For example, for $(LCO)_2+(LTO)_2$ on an STO substrate, the out of plane Co–O bond length between the CoO_2 planes [denoted as a bulklike Co–O bond in Fig. 1(c)] is 2.02 Å, while the bond length between the
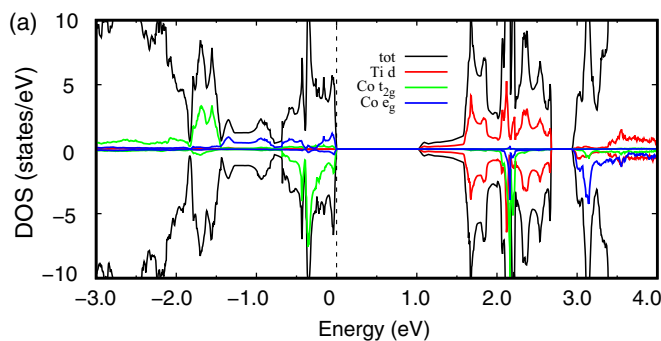

FIG. 2. Total (black) and projected (colors) density of states (DOS) of the $(LaCoO_3)_1+(LaTiO_3)_1$ superlattice onto the $3d$ orbitals of one Co atom. The Co atoms have high-spin states and AFM spin alignment, $U_{Co} = 3$ eV and $U_{Ti} = 3$ eV with GGA+U are used, and the in-plane lattice parameter is $a = 3.784$ Å. Positive and negative DOS describe spin-up and spin-down electronic states, respectively.
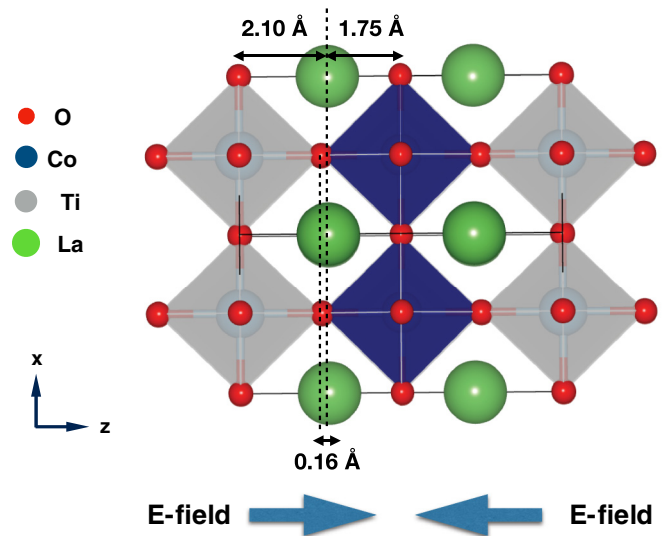

FIG. 3. Atomic structure of the $(LaCoO_3)_1+(LaTiO_3)_1$ superlattice with $a^0a^0a^0$ octahderal tilt and schematic picture of the local electric field. Distances between the La plane and the TiO_2 or CoO_2 plane as as well as the shift between La and O in the same plane (prior to displacement) are shown. The structure is obtained by using $U_{Co} = 3$ eV, $U_{Ti} = 2.5$ eV, GGA+U, and an in-plane lattice parameter of $a = 3.784$ Å.

CoO_2 and TiO_2 planes [denoted as an interfacial Co–O bond in Fig. 1(c)] is 2.28 Å, indicating that O^{2-} is shifted to the opposite direction of the local electric field.

In $(LTO)_1+(LCO)_1$, the CoO_6 octahedron faces interfaces on both sides. A simpler theoretical view of the structure, unencumbered by octahedral tilting, is afforded by considering $(LCO)_1+(LTO)_1$ with $a^0a^0a^0$ tilt within GGA+U whose structure is shown in Fig. 3. Here, the distance between the La^{3+} plane and the CoO_2 plane is 1.75 Å, while the distance between La^{3+} and TiO_2 plane is 2.10 Å.

3. Spin states of Co^{2+}

The HS state ($t_{2g}^5 e_g^2$) with $S = 3/2$ is depicted in Figs. 4(a) and 4(b): the spin-up Co $3d$ bands are fully occupied, while spin-down bands have two electrons in the t_{2g} channel. Due to the nonzero U_{Co}, the spin-down t_{2g} splits into two degenerate bands (d_{xz}, d_{yz}) under the Fermi level and one empty single band (d_{xy}) above the Fermi level, resulting in a Mott-like insulator. We find that $U_{Co} > 0$ is necessary for opening a energy gap for the HS state. In addition, the HS state is not even metastable at $U_{Co} = 0$: $U_{Co} > 2$ eV is needed (with $U_{Ti} = 3$ eV) to obtain a gapped and stable HS state. Regarding orbital polarization, the degeneracy of the t_{2g} manifold is already removed at $U_{Co} = 0$ because of the broken structural symmetry due to interface. This splitting between d_{xz}/d_{yz} and d_{xy} is further enhanced by imposed epitaxial strain and also enlarged by nonzero U_{Co}.

The LS state ($t_{2g}^6 e_g^1$) has $S = 1/2$ and is presented in Figs. 4(c) and 4(d): the t_{2g} bands are fully occupied, while the one remaining electron is in the e_g channel. The degeneracy of the e_g manifold is already broken at $U_{Co} = 0$ due to the interface formation and epitaxial strain. Due to the large
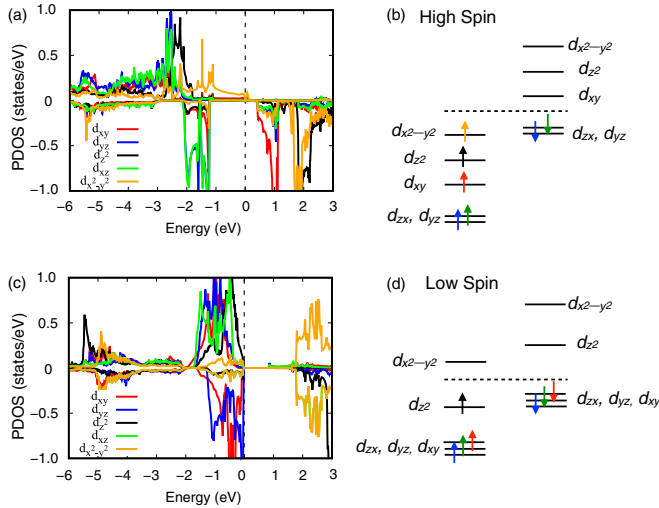
FIG. 4. Projected density of states of $(LaCoO_3)_1+(LaTiO_3)_1$ for (a) high-spin and (c) low-spin FM states. (b) and (d) Schematics of the corresponding atomic-like energy levels. $U_{Co} = 3$ eV and $U_{Ti} = 3$ eV with GGA+U are used, and the in-plane lattice parameter is $a = 3.784$ Å.

degeneracy splitting of the e_g bands, only the spin-up d_{z^2} is filled in the LS state while the spin-up $d_{x^2-y^2}$ and spin-down e_g bands are empty. As a result, the LS state is already insulating at $U_{Co} = 0$ and has strong e_g orbital polarization; $U_{Co} > 0$ enhances the orbital polarization and the energy gap.

4. Magnetic stability and effect of strain

There are two distinct Co atoms in our $(LTO)_1+(LCO)_1$ unit cell. Each Co can be HS or LS as well as spin-up or spin-down polarized. Therefore, there are six different spin configurations: ferromagnetic with two high-spin Co (HS FM), antiferromagnetic with two high-spin Co (HS AFM), ferromagnetic with one high-spin and one low-spin Co (HS/LS FM), ferrimagnetic with one high-spin and one low-spin Co (HS/LS FIM), ferromagnetic with two low-spin Co (LS FM), and antiferromagnetic with two low-spin Co (LS AFM).

As summarized by Fig. 5, HS AFM is most stable over a wide range of U_{Co}: $3.5 < U \leqslant 5$ eV for $a = 3.784$ Å, and $2.5 \leqslant U \leqslant 5$ eV for $a = 3.784$ and $a = 3.905$ Å. For a fixed Co spin state, HS AFM is more stable than HS FM, HS/LS FM is more stable than HS/LS FIM, and LS FM is more stable than LS AFM.

Interestingly, as shown in Fig. 5, the LS phase is stabilized by compressive strain whereas the HS phase is stabilized by tensile strain. In addition, both the HS FM and HS AFM phases are stabilized as U_{Co} increases. Certain combinations of strain and U_{Co} can drive magnetic transitions for the Co^{2+}: LS FM can be stabilized over HS AFM for compressive strain and low U_{Co} values, and an intermediate spin (HS/LS combination) state can become the ground state (e.g., $U_{Co} = 2.5$ eV and $a = 3.663$ Å). However, over broad ranges of parameters, it is the HS AFM that is the ground state. To the best of our knowledge, HS to LS or FM to AFM transitions have not been suggested or observed for Co^{2+} in bulk CoO, and this makes the LCO+LTO superlattice a potential test bed for modifying the spin state and magnetic interactions of Co^{2+} cations. We
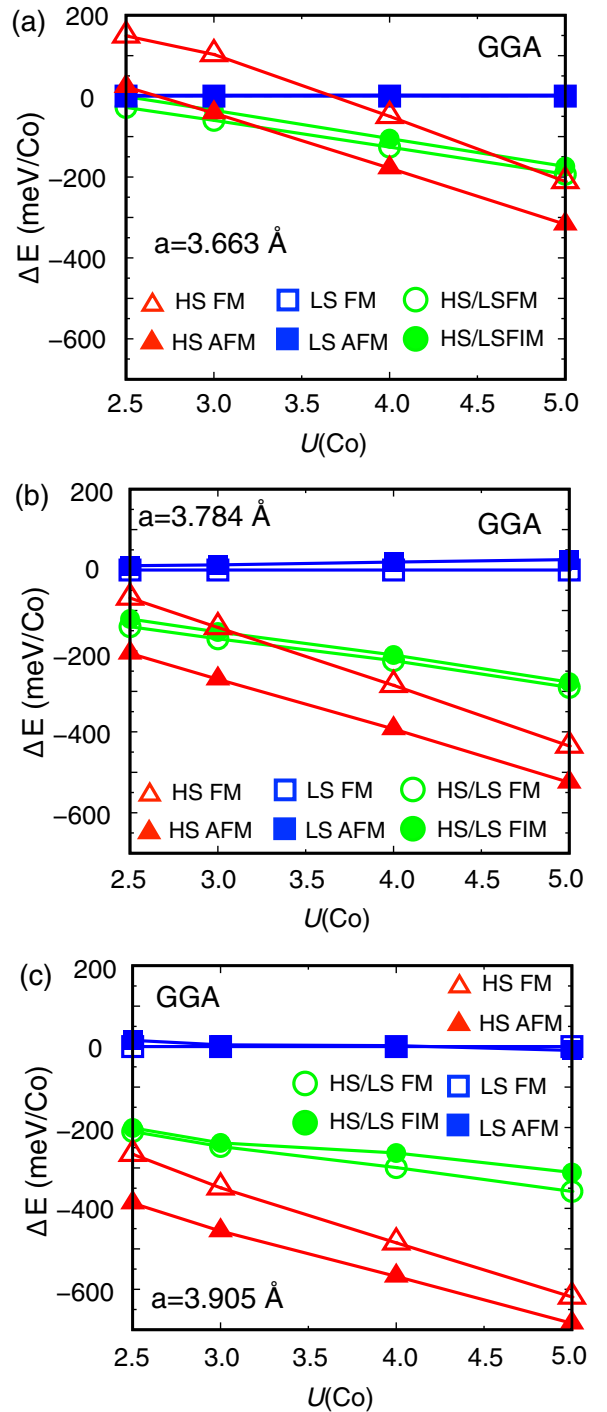

FIG. 5. U_{Co} dependence of the energies of different magnetic states of $(LTO)_1+(LCO)_1$ within GGA+U, for different in-plane lattice parameters (a) 3.663 Å, (b) 3.784 Å, and (c) 3.905 Å. Energies of LS FM phase are set to zero.

analyze the origin of the magnetic stability (Sec. IV A 3) and effect of strain (Sec. IV A 4) below.

5. Stabilization of ferromagnetism with hole doping

Electron or hole doping is a general and powerful way to change the magnetic stability of transition metal oxides such as cuprates [1,37] and manganites [38,39]. For Co, the
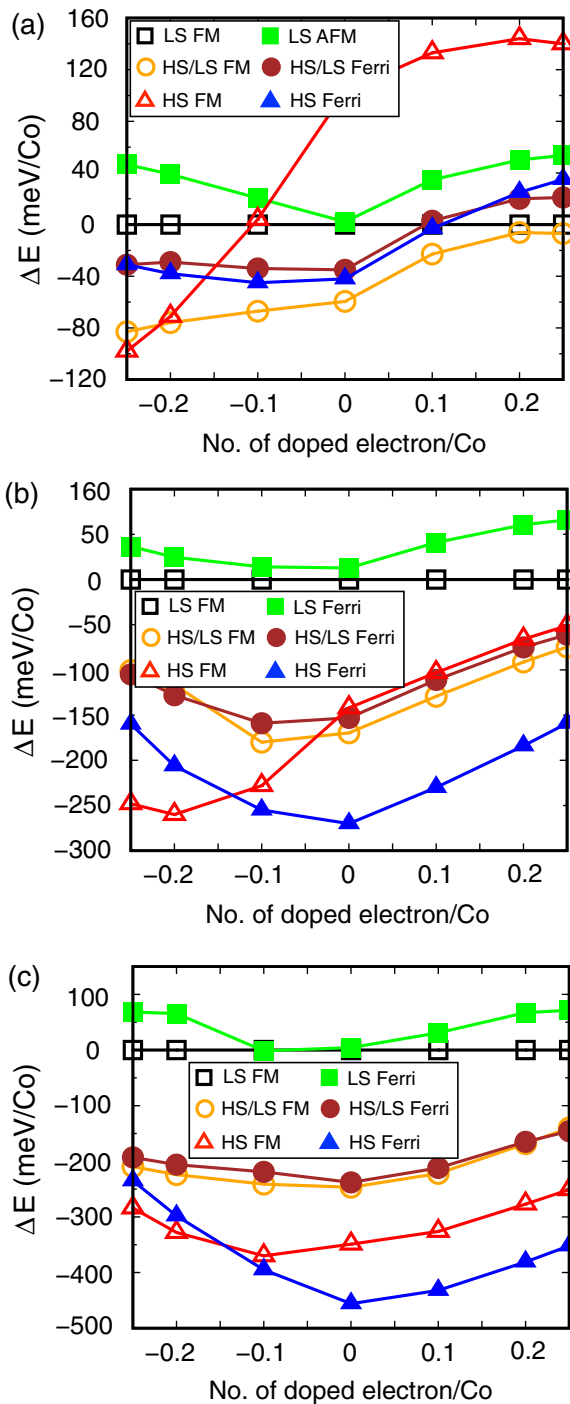
FIG. 6. Magnetic stabilities of electron- and hole-doped (LTO)$_1$+(LCO)$_1$ superlattices, with (a) $a = 3.663$ Å, (b) $a = 3.784$ Å, and (c) $a = 3.905$ Å. The energy of the LS FM phase is set to zero.

situation is more complex as a variety of spin states are possible, requiring a detailed analysis.

By manually changing total number of electrons in the supercell, both the spin state and the magnetic ordering can be changed via electron or hole doping in (LTO)$_1$+(LCO)$_1$ superlattices. In Fig. 6 we present the energies of six different phases as a function of electron/hole doping. The spin of

each Co cation is in fact different since the added electron or hole resides on one of the Co ions. Thus, what is referred to as an AFM alignment of Co spins is in fact a ferrimagnetic ordering, but for simplicity we refer to such phases by their parent undoped phase in Fig. 6.

The figure shows that the relative energetic stabilities are essentially unchanged by electron doping: the HS/LS FM phase is most stable at $a = 3.663$ Å [Fig. 6(a)], and the HS AFM phase is most stable at $a = 3.784$ Å and $a = 3.905$ Å [Figs. 6(b) and 6(c)] for all considered electron doping values. On the other hand, the relative magnetic stabilities are changed dramatically by hole doping: the energies of the hole-doped HS phases show large changes (red and blue curves in Fig. 6). The ferromagnetic HS FM phase becomes the ground state if the hole doping per Co is larger than ≈ 0.2, ≈ 0.13, and ≈ 0.15 for $a = 3.663$, 3.784, and 3.905 Å, respectively. This prediction is particularly interesting, because hole doping via Sr substitution on La sites should be much easier to achieve in LTO-based systems than electron doping. We analyze the doping effect in detail below (Sec. IV A 5) and show that the FM stabilization is driven by the double exchange mechanism. We note that the the presence of an AFM to FM transition with hoping is not obvious *a priori*: e.g., Fig. 6(a) shows that the LS state lacks any such transition while the HS state has a transition as a function of hole doping. To the best of our knowledge, magnetic systems comprised of Co^{2+} cations do not show ferromagnetism nor are they expected to display double exchange physics. We look forward to experimental verification of this prediction.

B. Key results for (LaCoO$_3$)$_2$+(LaTiO$_3$)$_2$ superlattice

Our computational supercells now contain four Co and four Ti. Since there is a great deal of shared physics between the 1+1 and 2+2 superlattices, we will briefly describe the main physical properties of the 2+2 superlattices while highlighting key differences: our overall approach and methods of analysis are identical for the two superlattices. The Co^{2+} cations in the (LCO)$_2$+(LTO)$_2$ superlattice can be HS or LS, similar to (LCO)$_1$+(LTO)$_1$, so that there are five possible configurations HS/LS ordering in the supercell as presented in top row of Fig. 7: all HS order (shortened to HS), A-type HS/LS order with ordering wave vector $\boldsymbol{q}_{sc} = (0, 0, \frac{1}{2})$ (A-HS/LS), C-type HS/LS order with $\boldsymbol{q}_{sc} = (\frac{1}{2}, \frac{1}{2}, 0)$ (C-HS/LS), G-type HS/LS order with $\boldsymbol{q}_{sc} = (\frac{1}{2}, \frac{1}{2}, \frac{1}{2})$ (G-HS/LS), and all LS order (LS). Separately, there are four possible orderings patterns for the Co magnetic moments: FM, A-type AFM, C-type AFM, and G-type AFM (see second row of Fig. 7). In total, we investigate all $5 \times 4 = 20$ distinct configurations.

We summarize the U_{Co}-dependent properties of the most relevant low-energy configurations in Fig. 8. For most choices of parameters, our full set data show that the HS G-type AFM phase is the ground state, except for the case of high compressive strain and small U_{Co} ($a = 3.663$ Å and $U_{Co} = 2.5$ eV) where we find that G-HS/LS A-AFM phase is more stable. To avoid excessive clutter, Fig. 8(a) shows data only for G-type AFM magnetic ordering. In general, the energies of the A-HS/LS, C-HS/LS, G-HS/LS phases lie between those of the LS and HS phases. For a fixed magnetic pattern [Figs. 8(a), 8(c), and 8(e)], the energy difference (ΔE) between LS and
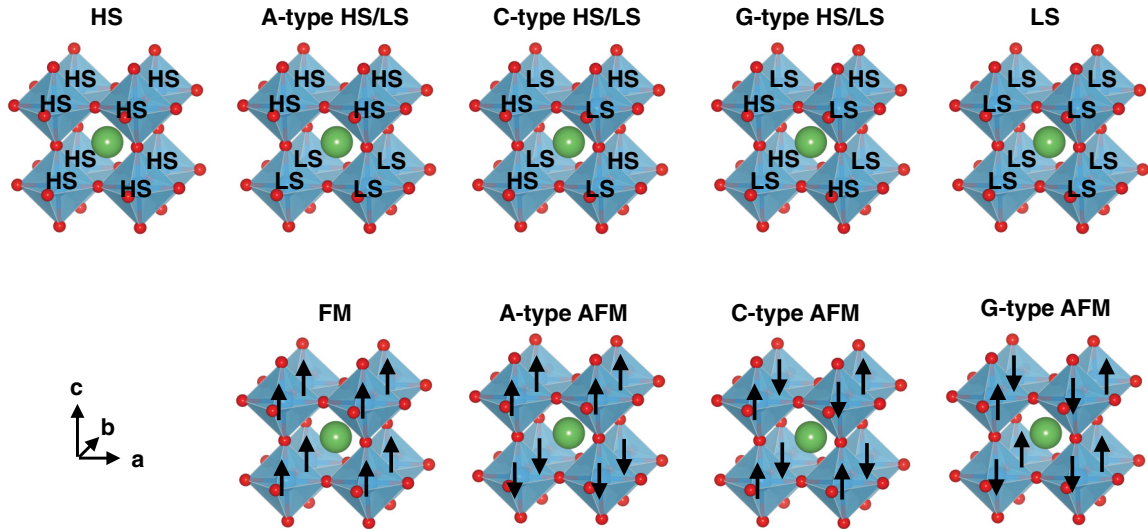
FIG. 7. Five possible HS/LS orderings and four possible magnetic orderings of the $(LaCoO_3)_2+(LaTiO_3)_2$ superlattice.

HS phases is enhanced as U_{Co} increases or as the in-plane lattice parameter a increases, both of which mirror the behavior of $(LTO)_1+(LCO)_1$.

In Figs. 8(b), 8(d), and 8(f), we compare the energies of different magnetic orderings as a function of U_{Co} when all then Co are in the HS state. The energies in this case obey the relations

$$E^{FM}[HS] > E^{A-AFM}[HS] > E^{C-AFM}[HS] > E^{G-AFM}[HS],$$

and, interestingly, this order holds for all U_{Co} and strain ranges considered. The origin of the magnetic stabilities are described in detail below (Sec. IV B).

IV. ANALYSIS OF SPIN STATES AND MAGNETIC STABILITY

In this section, we provide a detailed analysis of the electronic and magnetic properties of the $(LaCoO_3)_1+(LaTiO_3)_1$ and $(LaCoO_3)_2+(LaTiO_3)_2$ superlattices. Each subsection below deals with a particular physical effect or provides a microscopic model explaining the computed behaviors.

A. Analysis of $(LaCoO_3)_1+(LaTiO_3)_1$

As discussed in Sec. III A 4, there are two distinct Co atoms in our supercell of $(LTO)_1+(LCO)_1$. Since two Co atoms can be HS or LS separately, and also can be spin-up or spin-down separately, there are six different spin configurations as mentioned: ferromagnetic with two high-spin Co (HS FM), antiferromagnetic with two high-spin Co (HS AFM), ferromagnetic with one high-spin and one low-spin Co (HS/LS FM), ferrimagnetic with one high-spin and one low-spin Co (HS/LS FIM), ferromagnetic with two low-spin Co (LS FM), and antiferromagnetic with two low-spin Co (LS AFM). Among them, HS AFM is the most stable over a wide range of parameters, as shown in Fig. 9(a). For fixed spin states, HS AFM is more stable than HS FM [Fig. 10(a)], HS/LS FM is more stable than HS/LS FIM [Fig. 10(c)], and LS FM is more stable than LS AFM [Fig. 10(e)].

1. HS vs LS with fixed magnetic order: U_{Co} dependence

The above energy differences strongly depend on U_{Co}. Specifically, when the magnetic ordering is fixed to AFM, the energy difference between different spin states of Co increases monotonically as a function of U_{Co} as shown in Fig. 9(a).
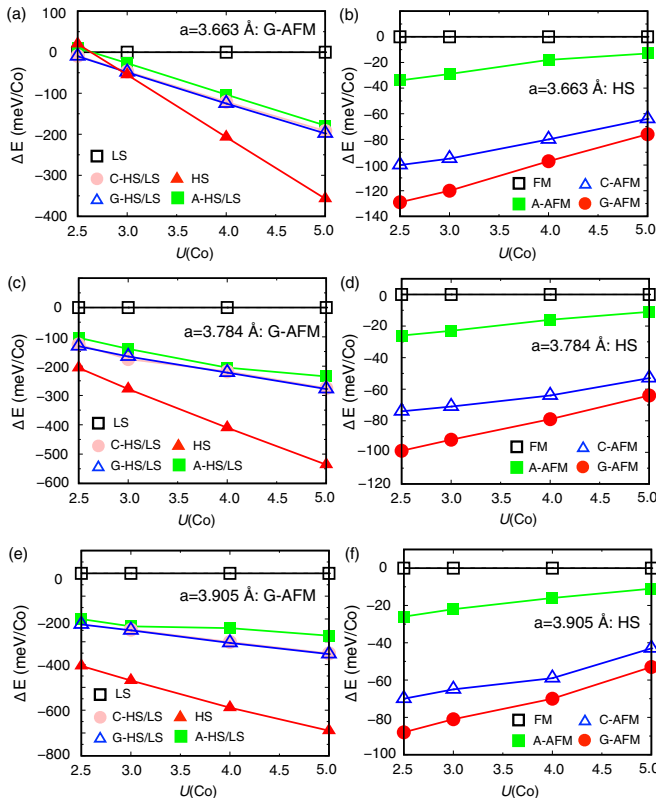

FIG. 8. U dependence of energies for different spin configurations of $(LTO)_2+(LCO)_2$ with different in-plane lattice parameters. Energy of LS FM is set to be zero.

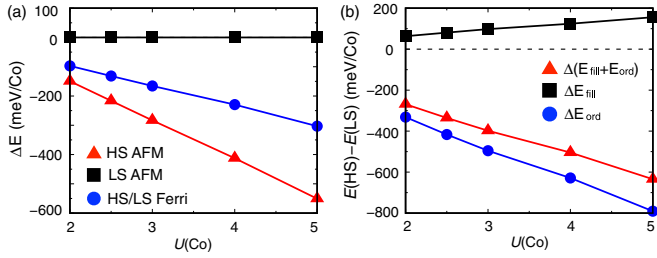FIG. 9. U_{Co} dependence of the total energies for AFM states of $(LTO)_1+(LCO)_1$ superlattices. (a) Total energies per Co of different magnetic configurations (the total energy of the LS state is chosen as the zero of energy). (b) Spectral decomposition of the $+U$ energy contribution (see text).

To explain this strong dependence, we analyze the difference $E[\text{HS AFM}]-E[\text{LS AFM}]$ by rewriting the DFT+U total energy as a spectral decomposition [40,41]

$$E = E_{\text{DFT}+U} = E_{\text{DFT}} + E_U - E_{\text{dc}}$$
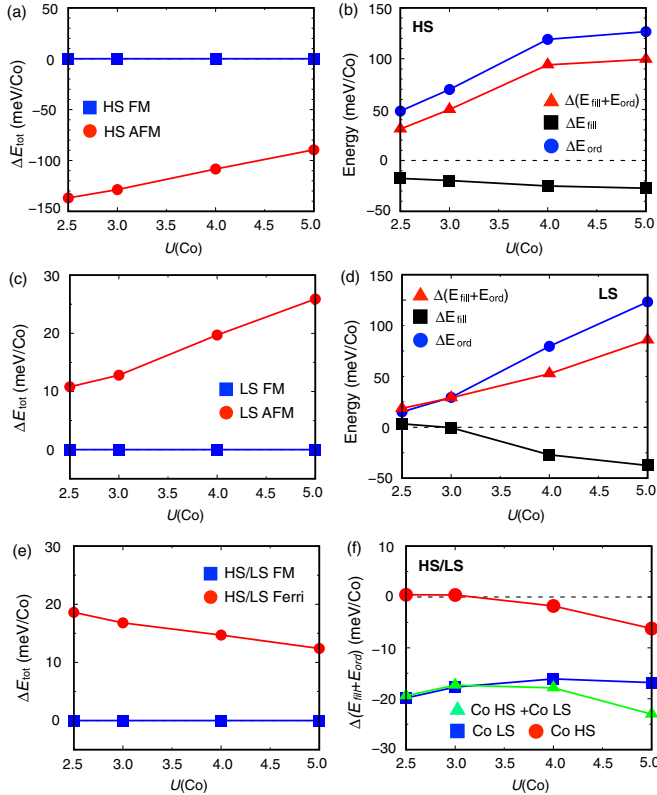$$= E_{\text{DFT}} + E_{\text{fill}} + E_{\text{ord}}, \quad (1)$$

FIG. 10. U_{Co} dependence of energies for different magnetic states of $(LTO)_1+(LCO)_1$. (a) energies of HS FM and HS AFM, where the energy of HS FM is set to be zero. (c) $\Delta E_{\text{fill}}[\text{HS}]$, $\Delta E_{\text{ord}}[\text{HS}]$, and $\Delta E_{\text{fill}}[\text{HS}] + \Delta E_{\text{ord}}[\text{HS}]$. (c) Energies of LS FM and LS AFM, where the energy of LS FM is set to be zero. (c) $\Delta E_{\text{fill}}[\text{LS}]$, $\Delta E_{\text{ord}}[\text{LS}]$, and $\Delta E_{\text{fill}}[\text{LS}] + \Delta E_{\text{ord}}[\text{LS}]$. (e) Energies of HS/LS FM and HS/LS FIM, where the energy of HS/LS FM is set to be zero. (f) $\Delta E_{\text{fill}}[\text{HS/LS}]$, $\Delta E_{\text{ord}}[\text{HS/LS}]$, and $\Delta E_{\text{fill}}[\text{HS/LS}] + \Delta E_{\text{ord}}[\text{HS/LS}]$.

where

$$E_{\text{fill}} = U(2l+1)\mu(1-\mu), \quad E_{\text{ord}} = -U(2l+1)\sigma^2. \quad (2)$$

Here $l = 2$ is the angular momentum of the atomic-like states for the DFT+U treatment, and μ and σ are the mean value and standard deviation of the eigenvalues of the single particle density matrix of the manifold of atomic-like orbitals (here Co $3d$ states). Within this spectral decomposition, the combined interaction and double counting energy simply depends on the two numbers μ and σ extracted from the local single-particle density matrix.

We define $\Delta E_{\text{fill}}^{\text{AFM}}$ and $\Delta E_{\text{ord}}^{\text{AFM}}$ via

$$\Delta E_{\text{fill}}^{\text{AFM}} = E_{\text{fill}}^{\text{AFM}}[\text{HS}] - E_{\text{fill}}^{\text{AFM}}[\text{LS}],$$
$$\Delta E_{\text{ord}}^{\text{AFM}} = E_{\text{ord}}^{\text{AFM}}[\text{HS}] - E_{\text{ord}}^{\text{AFM}}[\text{LS}], \quad (3)$$

and plot them versus U_{Co} in Fig. 9(b). While the change of $\Delta E_{\text{fill}}^{\text{AFM}}$ as a function of U_{Co} is relatively weak, $\Delta E_{\text{ord}}^{\text{AFM}}$ is the dominating contribution, similar to prior studies [40,41]. Therefore, the U_{Co} behavior is dictated largely by the difference in σ^2 of the two respective spin configurations. In other words, the orbital occupancy differentiation (i.e., orbital ordering) is more enhanced in the HS state than in the LS state as U_{Co} increases, and this enlarges the energy difference between them.

2. FM vs AFM for fixed Co spin state: U_{Co} dependence

Now we consider the energy difference between two magnetic configurations for fixed Co spin state. Figures 10(a) and 10(c) show that the energy difference between FM and AFM phases. While the energy difference between FM and AFM decreases as a function of U_{Co} for the HS state, this energy difference increases as a function of U_{Co} for the LS state which is the opposite trend. To explain these trends, we do a similar U_{Co}-dependent spectral analysis for $\Delta E[\text{HS}] = E^{\text{AFM}}[\text{HS}]-E^{\text{FM}}[\text{HS}]$ [Figs. 10(a) and 10(b)], $\Delta E[\text{LS}] = E^{\text{AFM}}[\text{LS}] - E^{\text{FM}}[\text{LS}]$ [Figs. 10(c) and 10(d)], and $\Delta E[\text{HS/LS}] = E^{\text{FIM}}[\text{HS/LS}] - E^{\text{FM}}[\text{HS/LS}]$ [Figs. 10(e) and 10(f)]. ΔE_{fill} and ΔE_{ord} are defined in a similar way as above: e.g.,

$$\Delta E_{\text{fill}}[\text{HS}] = E_{\text{fill}}^{\text{AFM}}[\text{HS}] - E_{\text{fill}}^{\text{FM}}[\text{HS}],$$
$$\Delta E_{\text{ord}}[\text{HS}] = E_{\text{ord}}^{\text{AFM}}[\text{HS}] - E_{\text{ord}}^{\text{FM}}[\text{HS}]. \quad (4)$$

Looking at the pair of Figs. 10(a) and 10(b) and the pair Figs. 10(c) and 10(d), the situation is very similar to that in the previous subsection: in both cases $\Delta E_{\text{fill}}[\text{HS}]$ is almost constant versus U_{Co} and relatively small in size while $\Delta E_{\text{ord}}[\text{HS}]$ dominates the behavior in that its increase with increasing U_{Co} explains the positive slope of $\Delta E[\text{HS}]$ or $\Delta E[\text{LS}]$.

We also considered the intermediate spin HS/LS FM and AFM (the latter is in fact ferrimagnetic as the moments are unequal) configurations where the unit cell contains one LS and one HS Co cation. As presented in Fig. 10(e), $\Delta E[\text{HS/LS}]$ varies by about 10 meV as U_{Co} changes from 2.5 to 5 eV. $\Delta(E_{\text{fill}} + E_{\text{ord}})[\text{HS/LS}]$ for the HS Co and the LS Co [see Fig. 10(f)] show opposing behaviors versus U_{Co} so their sum is relatively constant. As a result, the averaged value of $\Delta(E_{\text{fill}} + E_{\text{ord}})$ at $U = 2.5$ eV and $U = 5$ eV only differ by 12 meV.
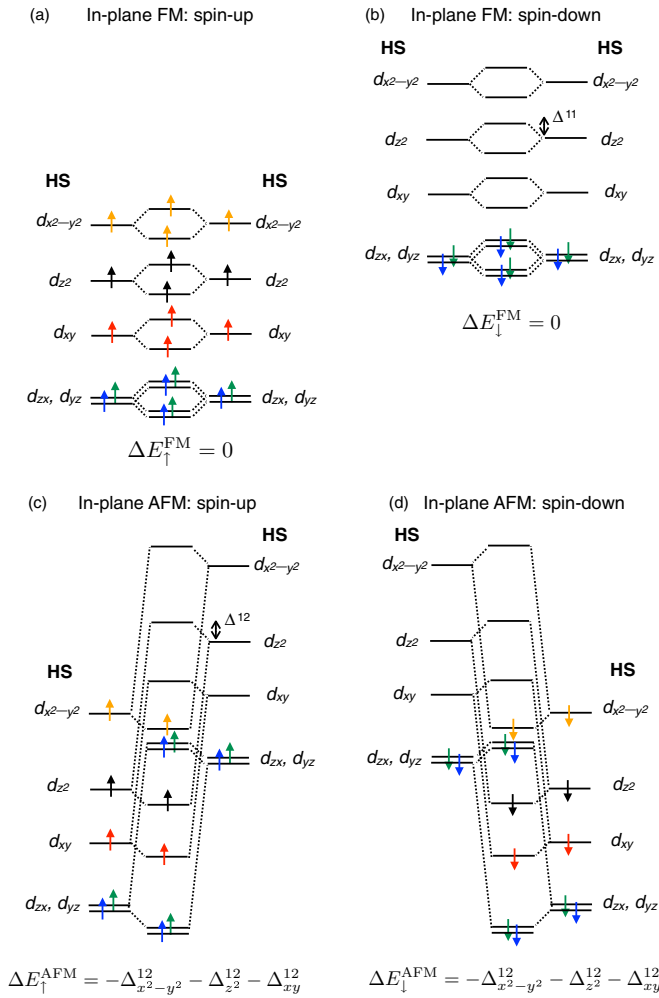
FIG. 11. Schematic molecular orbital view of Co $3d$ energy level diagrams and in-plane magnetic interactions between two neighboring HS Co^{2+} cations. (a) and (b) Two neighboring Co with FM alignment; (c) and (d) two neighboring Co with AFM alignment. Solid horizontal lines indicate energy levels; dashed lines indicate the effect of interactions; arrows indicate electron filling colored by orbital type. Δ^{11} and Δ^{12} are exchange splitting for FM and AFM configurations, respectively. ΔE is the energy lowering due to the magnetic interactions.

3. Origin of the magnetic stabilities

The above numerical observations of the relative magnetic stabilities require explanations. Here we will explain the origin of the magnetic energetics of (LTO)$_1$+(LCO)$_1$ using an energy band picture (i.e., molecular orbital theory) for three different spin configurations: HS, HS/LS, and LS.

Figure 11 shows the schematic energy diagram of for two in-plane HS Co neighbors with FM and AFM relative spin alignment. The interaction lines in this diagram do not indicate direct Co $3d$-Co $3d$ hybridization but instead the interaction mediated through the intervening O $2p$ states. The energetic position of the atomic-like energy levels are drawn based on analysis of projected densities of states diagrams such as Fig. 4.

The spin-up majority bands of HS FM are fully occupied, thus the Co-Co interactions do not lead to energetic stabilization as per Fig. 11(a) (i.e., both bonding and antibonding states are equally occupied). We note that the our Co cations have strong orbital degeneracy breaking whereby the t_{2g} d_{yz}/d_{zx} bands are lower in energy than the d_{xy} band is empty: in the minority-spin channel, the d_{yz}/d_{zx} bands are filled while the d_{xy} band is empty. As discussed in Sec. IV A, this splitting results a Mott-like insulating state. In the HS FM case, the minority-spin bands also do not lead to energetic stabilization: the $d_{yz}(d_{zx})$ spin-down on one Co only interact with the $d_{yz}(d_{zx})$ spin-down states on the neighboring Co, and as both are filled, there is no net lowering of energy as the bonding and antibonding states are again fully occupied [Fig. 11(b)]. Thus the energy lowering due to Co-Co interactions for HS FM is zero, $\Delta E^{\mathrm{FM}}[\mathrm{HS}] = 0$.

On the other hand, HS AFM Co-Co superexchange interactions lead to energetic stabilization [Figs. 11(c) and 11(d)]. While one Co has five spin-up and two spin-down electrons, the other Co has two spin-up and five spin-down electrons: d_{z^2}, d_{yz} and d_{zx} are fully occupied for both Co ions leading to no energy lowering; but the electrons in the majority-spin $d_{x^2-y^2}$ and d_{xy} states interact with empty counterparts on the other Co which leads to energy lowering (only bonding states become filled) as shown in Figs. 11(c) and 11(d). If we define the strength of the Co-Co interaction for one $3d$ orbital on one Co with the same orbital on the neighbor for the FM case as $-\Delta_d^{11}$ [see Fig. 11(b)] and for the AFM case as $-\Delta_d^{12}$ [see Fig. 11(c)], respectively, then the energy lowering of the spin-up channel in the AFM case is

$$\Delta E_{\uparrow}^{\mathrm{AFM}}[\mathrm{HS}] = -\Delta_{d_{x^2-y^2}}^{12} - \Delta_{d_{z^2}}^{12} - \Delta_{d_{xy}}^{12}. \quad (5)$$

The spin-down channel has same amount of the energy lowering. Therefore, within this model, the energy difference between HS FM and HS AFM can be written as

$$\Delta E[\mathrm{HS}] = \Delta E^{\mathrm{AFM}}[\mathrm{HS}] - \Delta E^{\mathrm{FM}}[\mathrm{HS}]$$
$$= -2\left(\Delta_{d_{x^2-y^2}}^{12} + \Delta_{d_{z^2}}^{12} + \Delta_{d_{xy}}^{12}\right), \quad (6)$$

which is negative as the Δ_d^{ij} are positive by our convention. Hence, this analysis provides a simple explanation of the stability of HS AFM compared to HS FM.

Figures 12(a) and 12(b) present the in-plane interactions between a HS Co and its neighboring LS Co for FM and FIM relative spin alignments. While the majority spin-up d bands of the HS Co are fully occupied, the $d_{x^2-y^2}$ spin-up band of the LS Co is empty [Fig. 12(a)] which leads to an energy lowering in the spin-up channel of $-\Delta_{d_{x^2-y^2}}^{11}$. In the minority spin-down channel, the d_{xy} band of the LS Co is occupied while the d_{xy} of the HS Co empty, creating a lowering of energy by $-\Delta_{d_{xy}}^{11}$. Thus, the total energy lowering for FM ordering of HS and LS neighboring Co is

$$\Delta E^{\mathrm{FM}}[\mathrm{HS/LS}] = -\Delta_{d_{x^2-y^2}}^{11} - \Delta_{d_{xy}}^{11}. \quad (7)$$

The case of ferrimagnetic (FIM) ordering between a HS Co and LS Co is shown in Figs. 12(c) and 12(d). For the spin-up channel, the HS $d_{x^2-y^2}$ and d_{z^2} are occupied but empty for the LS Co, leading to an energy lowering of $-\Delta_{d_{x^2-y^2}}^{12} - \Delta_{d_{z^2}}^{12}$; a
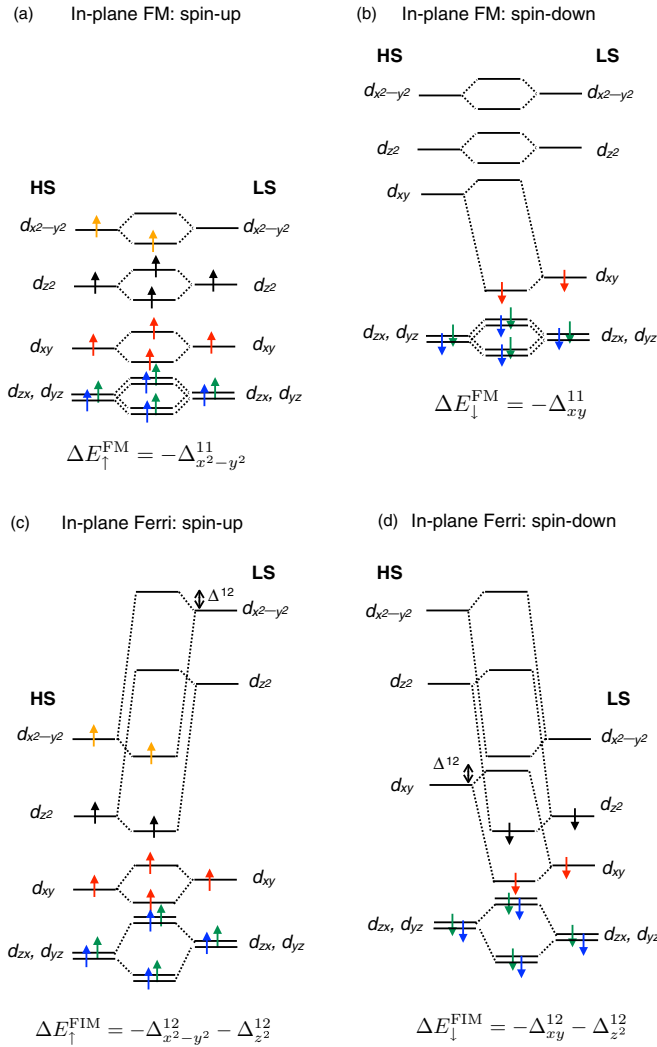
FIG. 12. Schematic diagram of the in-plane magnetic interaction between HS Co and LS Co.

FIG. 13. Schematic diagram of the in-plane magnetic interaction between LS Co and LS Co.

similar lowering happens for the low-spin channel due to d_{xy} and d_{z^2}. The total energetic stabilization for this FIM HS-LS case

$$\Delta E^{\mathrm{FIM}}[\mathrm{HS/LS}] = -2\Delta_{d_{z^2}}^{12} - \Delta_{d_{x^2-y^2}}^{12} - \Delta_{d_{xy}}^{12}. \qquad (8)$$

Hence, the energy difference between HS/LS FM and HS/LS FIM is thus

$$\Delta E[\mathrm{HS/LS}]$$
$$= \Delta E^{\mathrm{FM}}[\mathrm{HS/LS}] - \Delta E^{\mathrm{FIM}}[\mathrm{HS/LS}]$$
$$= -\left[\Delta_{d_{x^2-y^2}}^{11} - \Delta_{d_{x^2-y^2}}^{12}\right] - \left[\Delta_{d_{xy}}^{11} - \Delta_{d_{xy}}^{12}\right] + 2\Delta_{d_{z^2}}^{12}. \qquad (9)$$

For the $d_{x^2-y^2}$ and d_{xy} contributions, there is some partial cancellation between the Δ^{11} and Δ^{12} terms although these contributions should be net negative since FM interactions Δ^{11} take place between energy degenerate orbitals while the AFM Δ^{12} are between strongly exchange-split $3d$ orbitals leading to weaker interactions (i.e., homopolar versus heteropolar bonding in the language of semiconductors). However, with the addition of the positive contribution $2\Delta_{d_{z^2}}^{12}$, the
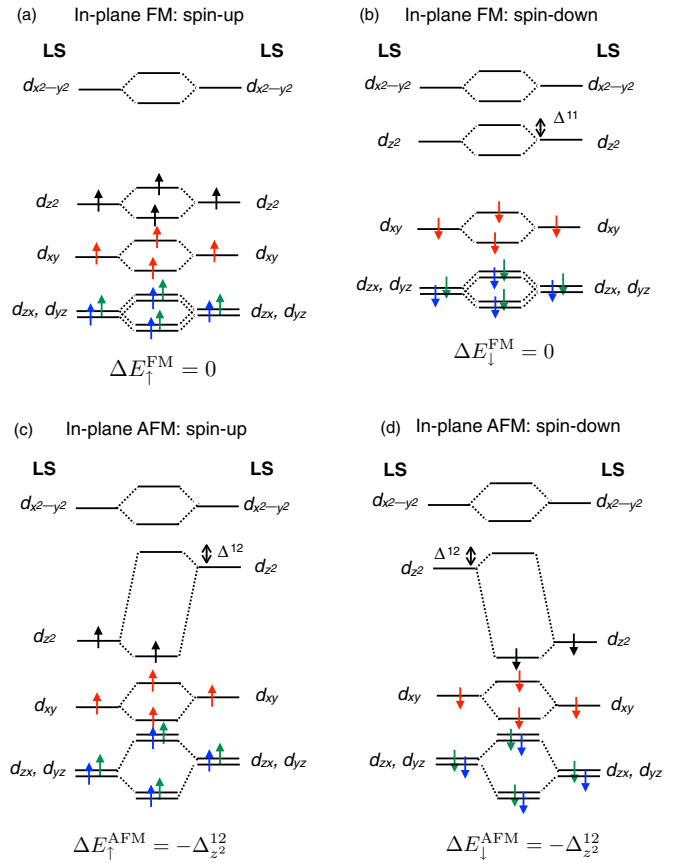
total is expected to be relatively small in magnitude, in agreement with the small energy differences shown in Fig. 10(e). Comparison to data in the figure shows that $\Delta^{11} > \Delta^{12}$ must be true so that FIM is higher in energy than FM.

Understanding the stability of the FM state for two LS Co neighbors, however, is more complicated. The simple band interaction picture cannot explain the data in Fig. 10(e), which show that LS FM is more stable than LS AFM: as per Fig. 13, the energy lowering of the FM configuration is zero while the AFM ordering should be lower in energy by $-2\Delta_{d_{z^2}}^{12}$. Furthermore, standard double exchange for FM configurations is unlikely to be a viable explanation since the system is not metallic (it has an energy gap) due to the large splitting between t_{2g} and e_g bands. Nor can Goodenough-Kanamori (GK)-type FM superexchange be the origin of the stability, because GK superexchange is maximum if $\angle$TM–O–TM=90° and cannot be applied for $\angle$TM–O–TM=180° [42–44]. We find that FM is also stable for the insulating undistorted $a^0a^0a^0$ phase, where Co–O–Co angle is 180°.

In the above analysis, we considered only the interaction between same d orbitals on the neighboring Co, e.g., d_{z^2}–d_{z^2} or d_{xy}–d_{xy}, since they are usually the dominant ones. The model predicted that the LS AFM state is stabilized by $-2\Delta_{d_{z^2}}^{12}$: but will be a very small quantity in this case since the exchange splitting of the d_{z^2} band is larger than 4 eV [see Fig. 4(b)] and we expect the hopping between the two
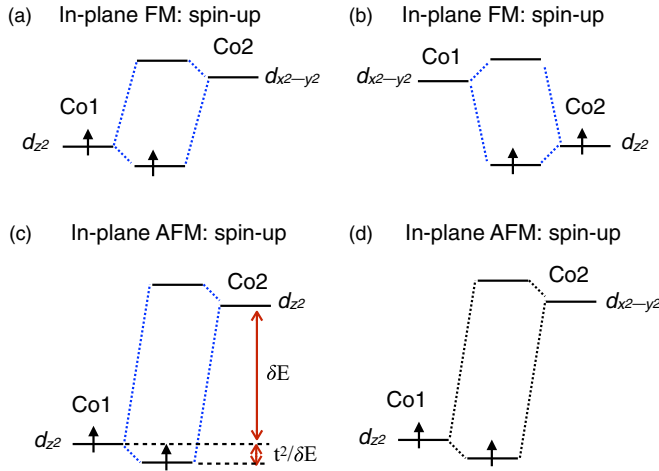
FIG. 14. Schematic magnetic interaction model between two neighboring LS Co for (a) and (b) FM spin order and (c) and (d) AFM spin order. Panel (c) shows the difference in on-site energy δE and how the hopping between the two orbitals t leads to an energetic lowering by $t^2/\delta E$ for the bonding state; numerical values are provided in Table I.
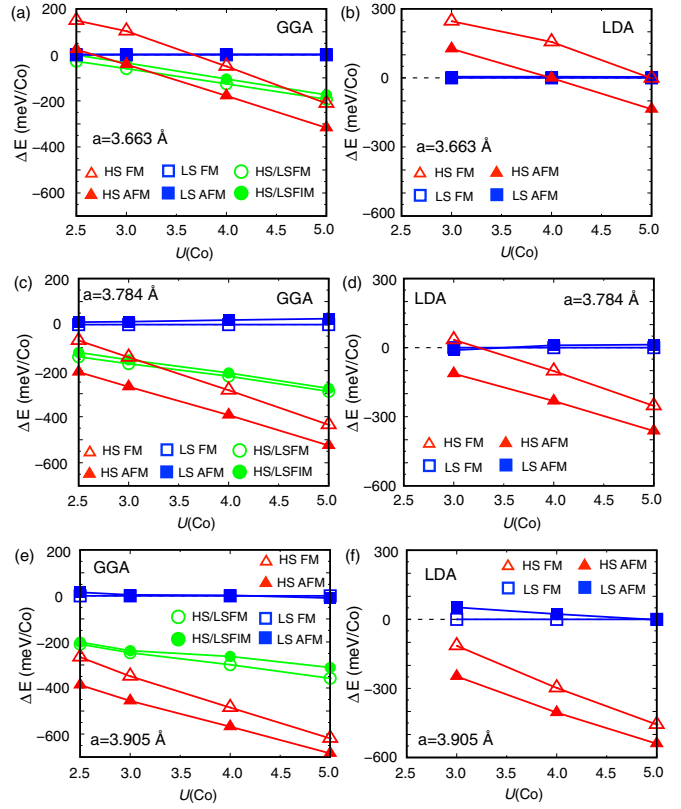

FIG. 15. U_{Co} dependence of the energies of different magnetic states of $(LTO)_1+(LCO)_1$ for different in-plane lattice parameters [3.663 Å for (a) and (b), 3.784 Å for (c) and (d), and 3.905 Å for (e) and (f)] and two different exchange-correlation functionals [(a), (c), and (e) for GGA+U and (b), (d), and (f) for LDA+U]. Energies of LS FM phase is set to zero. The energy of the FM phase is set to zero. Panels (a), (c), and (e) are the same as Fig. 5.

neighboring d_{z^2} orbitals to be small since they are strongly directional out-of-plane. Hence, it is likely that interactions between different orbitals on the neighboring Co can play a role in this case.

To capture the essence of the problem, we consider the ideal $a^0a^0a^0$ structure without octahedral tilts so the Co–O–Co bonding is along a straight line. In this case, the only symmetry allowed interactions that can lower the energy for the FM order are $d_{z^2}-d_{x^2-y^2}$ between neighboring atoms for the majority spin-up channel [Figs. 14(a) and 14(b)]. For AFM order, the relevant hoppings are $d_{z^2}-d_{z^2}$ (small and already discussed above) and $d_{z^2}-d_{x^2-y^2}$ in both spin channels as per Figs. 14(c) and 14(d).

We now create a more quantitative model by extracting on-site energies and hopping parameters for the LS FM and AFM cases by generating maximally localized Wannier functions (MWLFs) [33] that span the energy bands for the d_{z^2} and $d_{x^2-y^2}$ character bands near the Fermi level. These are low-energy or effective Wannier functions that are centered on the Co cations and span the space of the relevant bands (i.e., this is not a p-d model as we do not have any oxygen $2p$-like Wannier functions). Table I displays the key band parameters that describe the hoppings t between neighboring orbitals and their on-site energy differences δE. The energy lowering for an interacting pair of neighboring orbitals with a single

electron between them is estimated by perturbation theory to be $\Delta = -t^2/\delta E$. Table I shows that (a) the AFM $\Delta_{d_{z^2}}^{12}$ is indeed very weak because the hopping element t is so small, and (b) the FM $d_{z^2}-d_{x^2-y^2}$ interaction is more stabilizing due to the smaller energy splitting δE. We conclude that the LS FM state is more stable than LS AFM, and the stabilization is driven by more favorable $d_{z^2}-d_{x^2-y^2}$ interactions due to the smaller $d_{z^2}-d_{x^2-y^2}$ energy splitting in the FM case between Co neighbors.

4. Effect of strain and exchange-correlation functional

Given that the spin, orbital, and lattice degrees of freedom interact strongly in a perovskite transition metal oxygen octahedron, the electronic and magnetic properties of Co in $(LTO)_1+(LCO)_1$ depend on strain markedly. To study this, we consider the three different in-plane lattice parameters discussed above ($a = 3.663$ Å, 3.784 Å, and 3.905 Å). Within GGA+U for $U_{Co} = 3$ eV, these three lattice parameters corresponds to 3.7% compressive, 0.6% compressive, and and 2.6% tensile strain.

In Fig. 15 we summarize the strain-dependent stabilities of different spin states and magnetic orderings of Co within both GGA+U and LDA+U. As discussed in Sec. III A 4, the HS phases are stabilized greatly as the lattice parameter increases

TABLE I. Hopping parameters (t) and energy splitting of d_{z^2} and d_{z^2} bands (δE) as obtained from a Maximally Localize Wannier Function analysis.

Order	Interaction	δE (eV)	t (eV)	$t^2/\delta E$ (eV)
FM	$d_{z^2} - d_{x^2-y^2}$	2.04	−0.120	7.0×10^{-3}
AFM	$d_{z^2} - d_{z^2}$	3.38	−0.010	2.9×10^{-5}
AFM	$d_{z^2} - d_{x^2-y^2}$	2.98	−0.116	4.5×10^{-3}

[see Figs. 15(a), 15(c), and 15(e)]: the LS phase is stabilized by compressive strain, whereas the HS phase is stabilized by tensile strain. In addition, similar to the case of $a = 3.784$ Å discussed in detail above in Sec. IV A 1, HS FM and HS AFM phases are stabilized as U_{Co} increases [see Figs. 15(a), 15(c), and 15(e)]. Various combinations of strain and U_{Co} can drive magnetic transitions for the Co^{2+}: LS FM can be stabilized over the HS AFM for compressive strain and low U_{Co} and an intermediate spin (HS/LS combination) state can become the ground state (e.g., $U_{Co} = 2.5$ eV and $a = 3.663$ Å). However, over broad ranges of parameters, it is the HS AFM that is the ground state. To the best of our knowledge, HS to LS or FM to AFM transitions have not been suggested or observed for Co^{2+} in bulk CoO, and this makes the LCO+LTO superlattice a potential test bed for modifying the spin state and magnetic interactions of Co^{2+} ions.

Analysis of the results of Fig. 15 show that the U_{Co} dependence of the energy difference between HS and LS phases originates from the orbital occupancy differentiation energy E_{ord} [Eq. (2)] much like what was shown in Fig. 9. On the other hand, we do not find that the relative stabilization of the LS phase for compressive strain is connected to the atomic-like $+U$ contributions to the total energy E_{ord} nor E_{fill} but must instead originate from the underlying DFT energy E_{DFT} that encodes the electronic dispersion and hopping contributions. The idea that the DFT part of the total energy controls the relative stability of the LS phase means that its stability should strongly depend on the choice of DFT functional. This is borne out by Fig. 15 which compares the GGA and LDA functionals. The trends versus U_{Co} and strain are very similar between the two functionals, but the energy of the HS phases is shifted upwards compared to the LS phases as we switch from GGA to LDA.
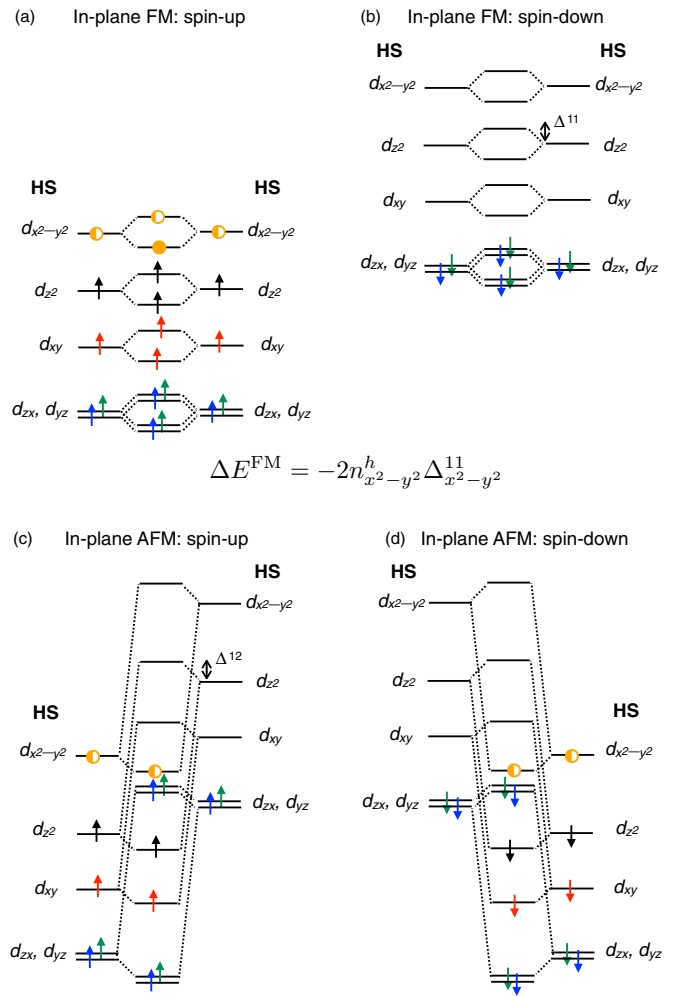
5. Effect of doping

Here we analyze the origin of the ferromagnetic stability with hole doping, which is discussed in Sec. III A 5. As described above, we find that both the spin state and the magnetic ordering can be changed via electron or hole doping in (LTO)$_1$+(LCO)$_1$ superlattices.

To understand these results, we begin with the fact that both the electron-doped and hole-doped HS phases become metallic in our calculations. Doped electrons partially occupy the minority spin-down d_{xy} states, and doped holes resides on majority spin-up d_{z^2} and $d_{x^2-y^2}$ states. Given the metallicity of the hole-doped state, the stability of the FM ordering turns out to be due to the double exchange mechanism.
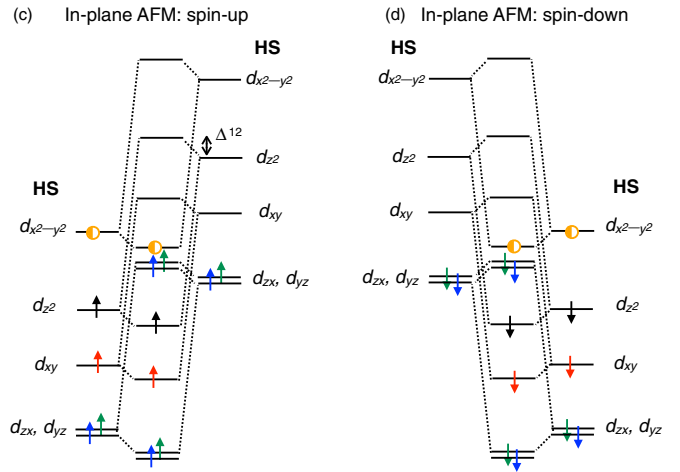
We use the schematic band interaction diagrams of in Fig. 16 to explain this stabilization mechanism. As per Fig. 16(a), the energy lowering of FM HS ordering is nonzero because of the holes in majority spin-up d_{z^2} and $d_{x^2-y^2}$ bands. Defining the number of holes as $n^h_{d_{z^2}}$ and $n^h_{d_{x^2-y^2}}$, the energy lowering of the FM ordering is

$$\Delta E^{FM} = -2n^h_{x^2-y^2}\Delta^{11}_{x^2-y^2}, \quad (10)$$

where the factor of two is due to the holes on both neighboring Co migrating to the shared antibonding $d_{x^2-y^2}$ state. The energy lowering of the AFM ordering (strictly speaking, it is

$$\Delta E^{FM} = -2n^h_{x^2-y^2}\Delta^{11}_{x^2-y^2}$$

$$\Delta E^{AFM} = -2(1 - n^h_{x^2-y^2})\Delta^{12}_{x^2-y^2} - 2\Delta^{12}_{z^2} - 2\Delta^{12}_{xy}$$

FIG. 16. Schematic diagram of the in-plane magnetic interaction between two neighboring HS Co and HS Co for FM (a) and (b) and AFM (c) and (d) configurations in hole-doped (LTO)$_1$+(LCO)$_1$. Full electronic occupation of a state is indicated by an arrow of filled circle, while partial occupation or presence of holes is indicated by the half-filled circles.

ferrimagnetic as explained above) is

$$\Delta E^{AFM} = -\left(2 - 2n^h_{x^2-y^2}\right)\Delta^{12}_{x^2-y^2} - 2\Delta^{12}_{z^2} - 2\Delta^{12}_{xy}. \quad (11)$$

The energy difference between the two phases is thus

$$\Delta E^{FM} - \Delta E^{AFM} = -2n^h_{x^2-y^2}\left(\Delta^{11}_{x^2-y^2} + \Delta^{12}_{x^2-y^2}\right) + 2\left(\Delta^{12}_{xy} + \Delta^{12}_{x^2-y^2} + \Delta^{12}_{z^2}\right). \quad (12)$$

This energy difference can change sign with increasing hole doping $n^h_{d_{x^2-y^2}}$. Furthermore, since Δ^{11}_d energies are much larger than Δ^{12}_d energies, the value of $n^h_{d_{x^2-y^2}}$ at which it changes sign should be small, in agreement with our numerical findings.
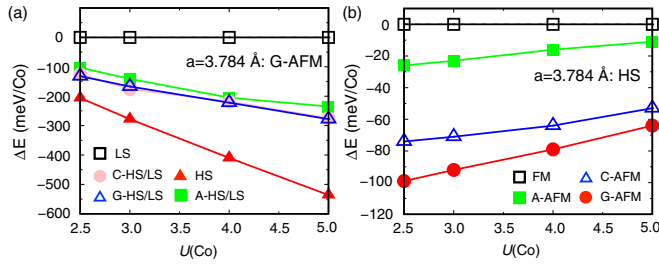
FIG. 17. U dependence of energies for different spin configurations of $(LTO)_2+(LCO)_2$ with lattice parameter $a = 3.784$. Energy of LS FM is set to be zero. (a) and (b) are same as Figs. 8(c) and 8(d).

B. Analysis of $(LaTiO_3)_2+(LaCoO_3)_2$

We now turn to analyze the electronic and magnetic properties of $(LCO)_2+(LTO)_2$ superlattices, which are briefly discussed in Sec. III B. As in Sec III B, there is a great deal of shared physics between the 1+1 and 2+2 superlattices, thus we will only describe the main physical properties of the 2+2 superlattices while highlighting key differences: our overall approach and methods of analysis are identical for the two superlattices.

There are five possible configurations HS/LS ordering in the $(LCO)_2+(LTO)_2$ supercell, as we already discussed in Sec. III B and top row of Fig. 7: all HS order (shortened to HS), A-type HS/LS order (A-HS/LS), C-type HS/LS order (C-HS/LS), G-type HS/LS order (G-HS/LS), and all LS order (LS). Separately, there are four possible orderings patterns for the Co magnetic moments: FM, A-type AFM, C-type AFM, and G-type AFM (see second row of Fig. 7). In total, we investigate all $5 \times 4 = 20$ configurations.

As discussed in Sec. III B, HS G-AFM is the ground state for most choices of parameters (see Fig. 8 or 17), and the energies of the A-HS/LS, C-HS/LS, G-HS/LS phases lie between those of the LS and HS phases. For a fixed magnetic pattern [Figs. 8(a), 8(c), and 8(e)], the energy difference (ΔE) between LS and HS phases is enhanced as U_{Co} increases or in-plane lattice parameter a increases which is similar to the behavior of $(LTO)_1+(LCO)_1$. Again, like the behavior of the 1+1 superlattices described in Sec. IV A 1, the U_{Co} dependence of ΔE for 2+2 superlattices turns out to be explained by the behavior of the ordering energy ΔE_{ord} [Eqs. (1) and (2)] between LS and HS phases.

As mentioned in Sec. III B, the energies different magnetic orderings obey the relations

$$E^{FM}[HS] > E^{A\text{-}AFM}[HS] > E^{C\text{-}AFM}[HS] > E^{G\text{-}AFM}[HS],$$

and interestingly this order holds for all U_{Co} and strain ranges considered.

As described in Fig. 11 and its associated discussion, in-plane magnetic interactions stabilizes AFM spin alignment, thus $E^{FM}[HS]$ and $E^{A\text{-}AFM}[HS]$ are above $E^{C\text{-}AFM}[HS]$ and $E^{G\text{-}AFM}[HS]$.

In order to explain why $E^{FM}[HS] > E^{A\text{-}AFM}[HS]$ and $E^{C\text{-}AFM}[HS] > E^{G\text{-}AFM}[HS]$, i.e., the stability AFM order along the out-of-plane direction, we examine the out-of-plane magnetic interaction for the HS phase in Fig. 18. In the out-of-plane direction, only d_{z^2}, d_{zx}, and d_{yz} on two neighboring Co will interact significantly. While the FM
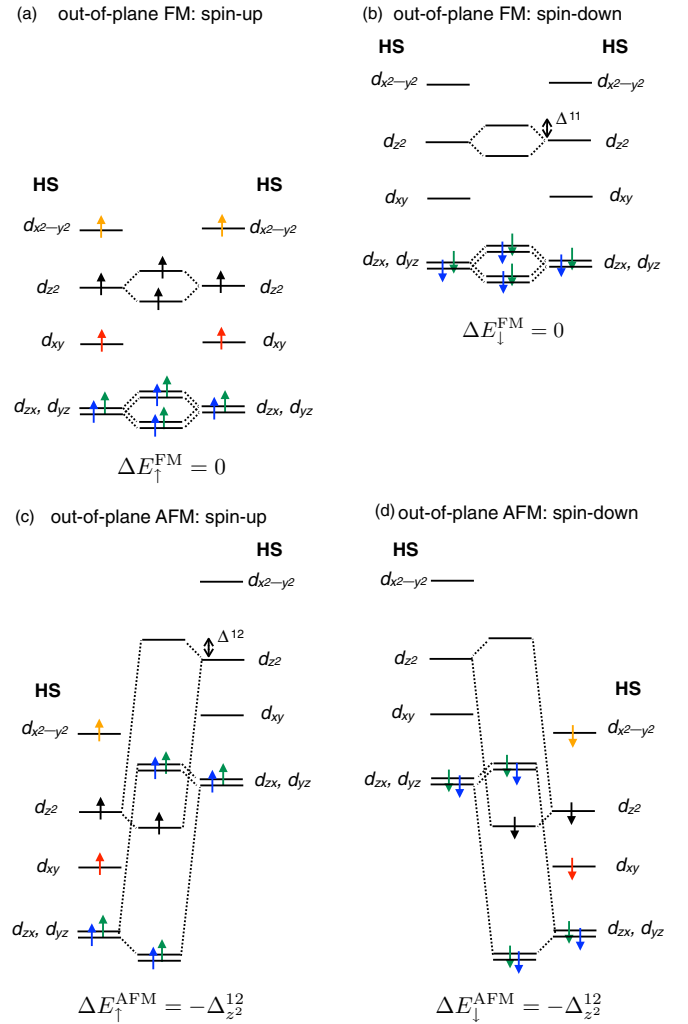

FIG. 18. Schematic diagram of the out-of-plane magnetic interaction between HS Co and HS Co.

alignment has no net energy lowering due to out-of-plane interactions [see Figs. 18(a) and 18(b)], the interactions between the d_{z^2} on the two Co lowers the energy by $-2\Delta_{d_{z^2}}^{12}$ for AFM alignment [Figs. 18(c) and 18(d)]. The energy difference between the FM and AFM configurations due to out-of-plane interactions is

$$\Delta E[HS] = \Delta E^{AFM}[HS] - \Delta E^{FM}[HS] = -2\Delta_{d_{z^2}}^{12}, \quad (13)$$

so that we expect $E^{AFM}[HS] < E^{FM}[HS]$ and $E^{G\text{-}AFM}[HS] < E^{C\text{-}AFM}[HS]$.

V. SUMMARY AND OUTLOOK

LCO+LTO superlattices show strong electron transfer, significant structural distortion, and robust orbital polarization. For a wide range of computational parameters, we predict high-spin Co and a checkerboard antiferromagnetic (AFM) order on the Co superlattice (2D checkerboard for the 1+1 superlattice and 3D checkerboard, i.e., G-type, for the 2+2 superlattice). A detailed analysis of the electronic structure reveals how superexchange interactions control the stability of

the magnetic orders. Finally, hole doping of the superlattices can lead to stabilization of a ferromagnetic ground state of Co^{2+}. This is unexpected and interesting especially for future experiments. Generally, materials containing Co^{2+} as the sole magnetic cation, such as CoO or Co_3O_4 (which also contains nonmagnetic Co^{3+} [45]), show antiferromagnetic ordering. A ferrimagnetic compound such as $CoFe_2O_4$ contains Fe^{3+} at the A sites and Fe^{3+}/Co^{2+} at B sites which are aligned antiferromagnetically [46]. Hence, the ability to create a ferromagnet using high-spin Co^{2+} is a new and, in our mind, surprising prediction.

Experimentally, we hope to see verification of the checkerboard AFM order of these superlattices. Even more exciting will be the experimental realization of ferromagnetism via hole doping through replacement of La by Sr; by careful control of the doping, the FM and AFM order can be made nearly degenerate in energy, potentially leading to interesting magnetic response and new magnetic phases.

Theoretically, more advanced models such as DFT+dynamical mean field theory can be used to verify the predictions made here using GGA+U. Furthermore, understanding the origin of the orbital polarization in these charge-transfer systems is interesting in terms of basic science as well as electronic engineering. Finally, investigation of thicker LCO layers in the superlattice, i.e., $(LTO)_2+(LCO)_n$ for $n \geqslant 3$, should prove interesting as well, since the interaction between Co^{2+} at the interface and Co^{3+} at the bulklike region may lead to other unexpected physical phenomena.

APPENDIX: U DEPENDENCE OF $LaCoO_3$ AND CoO

Here we aim to obtain optimal U_{Co} value for Co^{2+} in the LCO+LTO superlattices by studying bulk $LaCoO_3$ (Co^{3+}) and CoO (Co^{2+}). Below, we will show that the experimental nonmagnetic ground state for $LaCoO_3$ is stable with $U_{Co} \leqslant$ 2.5 eV for $LaCoO_3$, while $U_{Co} \sim 4.5$ eV is needed to obtain the experimental band gap of bulk CoO (see Fig. 19). We will conclude that $U_{Co} = 3$ eV is a reasonable value.

1. Bulk $LaCoO_3$ (LCO)

We consider the energetics of different magnetic configurations of Co^{3+} in LCO. We begin with bulk $LaCoO_3$ within both GGA+U and LDA+U for $0 \leqslant U_{Co} \leqslant 5$ eV with the $R\bar{3}c$ crystal structure, with a unit cell containing two Co atoms. The atomic structures and lattice vectors are fully relaxed. As presented in Figs. 19(a) and 19(b) and Table II, we can stabilize five different Co^{3+} spin states: $S = 0$, 1/2, 1, 1#2, and 2. The $S = 1$ and $S = 1$#2 configurations have same total spin, but magnetic moments of each Co atom in the
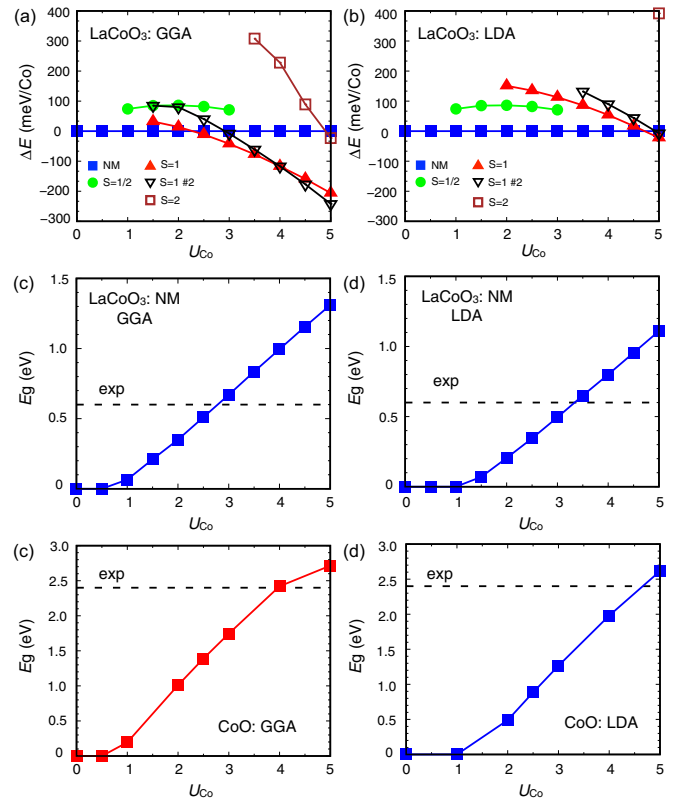

FIG. 19. Total energies of different magnetic states of bulk $LaCoO_3$ within (a) GGA+U and (b) LDA+U, and the band gap of bulk $LaCoO_3$ within (c) GGA+U and (d) LDA+U. Band gap of bulk CoO within (e) GGA+U and (f) LDA+U. The total energies of the nonmagnetic insulating phase (NM) are set to zero.

supercell are differ (See Table II). Interestingly, $S=1/2$, 1, and 1#2 show charge, spin, and bond length disproportionation (see Table II), while their structural symmetry is still $R\bar{3}c$. For example, for $S=1$, the two Co atoms (Co1 and Co2) have different total numbers of d electrons (N_d) and Co magnetic moments (M), in addition to different Co–O bond lengths d_{Co-O}: $N_d(Co1) = 7.349$ with $d_{Co1-O} = 1.90$ Å while $N_d(Co2) = 7.047$ with $d_{Co2-O} = 1.98$ Å.

Within GGA+U [Fig. 19(a)], the ground state of bulk $LaCoO_3$ within GGA+U is $S = 0$ (nonmagnetic state, NM) for $0 \leqslant U_{Co} < 2.5$ eV, $S = 1$ for $2.5 \leqslant U_{Co} < 4$ eV, and

TABLE II. Magnetic moment M (μ_B) and N_d of Co1 and Co2 in bulk $LaCoO_3$. $U_{Co} = 2.5$ eV is used, except for the case $S = 2$ since this state is not even metastable when $U_{Co} < 3.5$ eV. M and N_d are computed from the VASP-calculated local $3d$ occupancies around each atom.

	M(Co) (μ_B)		N_d(Co)	
	Co1	Co2	Co1	Co2
(i) $S = 0$ (NM)	0	0	7.332	7.332
(ii) $S = 1/2$	0.344	1.795	7.375	7.219
(iii) $S = 1$	0.366	2.922	7.349	7.047
(iv) $S = 1$#2	1.545	2.322	7.222	7.196
(v) $S = 2$	3.224	3.224	6.956	6.956

$S = 1$#2 for $4 \leqslant U_{Co} \leqslant 5$ eV. Thus, within GGA+U, $0 \leqslant U_{Co} < 2.5$ eV is appropriate to reproduce the nonmagnetic low-temperature ground state in the experiment. Within LDA+U, the $S = 0$ NM state is the ground state for $0 \leqslant U_{Co} \leqslant 4.5$ eV.

In addition to the energetics of the various spin states, we also consider the band gap (E_g) of bulk LaCoO$_3$. As summarized in Fig. 19(c), E_g within GGA+U with $U = 2.5$ eV and $U = 3$ eV are 0.51 and 0.67 eV, respectively, which are both close to the the experimental gap of ≈ 0.6 eV [47]. Within LDA+U, $U = 3.5$ eV gives $E_g = 0.65$ eV, as shown in Fig. 19(d).

Considering both the nature of the magnetic ground state and a reasonable value of the energy gap, we conclude that $U = 2.5$ eV within GGA+U and $U = 3.5$ eV within LDA+U are reasonable values for studying bulk LaCoO$_3$. Our U values are comparable to those from previous DFT+U studies: $U_{Co} - J_{Co} = 2.7$, 3.5, and 4.5 eV [15] or LDA+U values of $U_{Co} = 7.8$ eV and $J_{Co} = 0.92$ eV [13].

2. Bulk CoO

In the LaCoO$_3$+LaTiO$_3$ superlattice, the electron transfer from Ti to Co will lead to a 2+ charge state for Co (see the

next section). Therefore, we also calculate the U_{Co} dependence of the band gap of bulk CoO which also contains Co^{2+}.

At low temperature, bulk CoO is antiferromagnetic with wave vector $\boldsymbol{q}_{fcc} = (\frac{1}{2}, \frac{1}{2}, \frac{1}{2})$ [21,22], and an insulator with energy gap $E_g = 2.4$ eV [20]. In Figs. 19(c) and 19(d) we plot E_g of CoO as a function of U_{Co}. $U_{Co} = 4$ eV within GGA+U and $U_{Co} \sim 4.8$ eV within LDA+U give the experimental gap. These values are similar to the previous GGA+U results: $E_g = 2$ eV with $U_{Co} - J_{Co} = 3.3$ eV [48], $E_g = 2.8$ eV with $U_{Co} = 7.1$ eV and $J_{Co} = 1$ eV [48].

3. Choosing U_{Co}

Within GGA+U, we need $U_{Co} = 2.5$ eV for bulk LaCoO$_3$ to be described well, and $U_{Co} = 4$ eV for bulk CoO. Since we expect out superlattice to contain Co^{2+} which is more similar to CoO, we choose $U_{Co} = 3$ eV unless otherwise specified. Below, we will explore $0 \leqslant U_{Co} \leqslant 5$ eV to study the U dependence of the electronic and magnetic properties. We consider $U_{Ti} = 0$, 3, and 5 eV, and use $U_{Ti} = 3$ eV unless specified otherwise. This value of U_{Ti} is obtained by fitting the optical gap of LaTiO$_3$ to be 0.2 eV based on our previous work [49].

[1] P. A. Lee, N. Nagaosa, and X.-G. Wen, Rev. Mod. Phys. **78**, 17 (2006).

[2] Y. Tokura and N. Nagaosa, Science **288**, 462 (2000).

[3] H. Y. Hwang, Y. Iwasa, M. Kawasaki, B. Keimer, N. Nagaosa, and Y. Tokura, Nat. Mater. **11**, 103 (2012).

[4] V. G. Bhide, D. S. Rajoria, G. R. Rao, and C. N. R. Rao, Phys. Rev. B **6**, 1021 (1972).

[5] C. Zobel, M. Kriener, D. Bruns, J. Baier, M. Grüninger, T. Lorenz, P. Reutler, and A. Revcolevschi, Phys. Rev. B **66**, 020402(R) (2002).

[6] K. Asai, O. Yokokura, N. Nishimori, H. Chou, J. M. Tranquada, G. Shirane, S. Higuchi, Y. Okajima, and K. Kohn, Phys. Rev. B **50**, 3025 (1994).

[7] M. Itoh, I. Natori, S. Kubota, and K. Motoya, J. Phys. Soc. Jpn. **63**, 1486 (1994).

[8] R. H. Potze, G. A. Sawatzky, and M. Abbate, Phys. Rev. B **51**, 11501 (1995).

[9] T. Saitoh, T. Mizokawa, A. Fujimori, M. Abbate, Y. Takeda, and M. Takano, Phys. Rev. B **55**, 4257 (1997).

[10] K. Asai, A. Yoneda, O. Yokokura, J. M. Tranquada, G. Shirane, and K. Kohn, J. Phys. Soc. Jpn. **67**, 290 (1998).

[11] S. Yamaguchi, Y. Okimoto, and Y. Tokura, Phys. Rev. B **55**, R8666 (1997).

[12] A. I. Liechtenstein, V. I. Anisimov, and J. Zaanen, Phys. Rev. B **52**, R5467 (1995).

[13] M. A. Korotin, S. Y. Ezhov, I. V. Solovyev, V. I. Anisimov, D. I. Khomskii, and G. A. Sawatzky, Phys. Rev. B **54**, 5309 (1996).

[14] K. Knížek, P. Novák, and Z. Jirák, Phys. Rev. B **71**, 054420 (2005).

[15] K. Knížek, Z. Jirák, J. Hejtmánek, and P. Novák, J. Phys.: Condens. Matter **18**, 3285 (2006).

[16] M. Zhuang, W. Zhang, and N. Ming, Phys. Rev. B **57**, 10705 (1998).

[17] Z. Ropka and R. J. Radwanski, Phys. Rev. B **67**, 172401 (2003).

[18] S. W. Biernacki, Phys. Rev. B **74**, 184420 (2006).

[19] B. Chakrabarti, T. Birol, and K. Haule, Phys. Rev. Mater. **1**, 064403 (2017).

[20] R. Zimmermann, P. Steiner, R. Claessen, F. Reinert, S. Hüfner, P. Blaha, and P. Dufek, J. Phys.: Condens. Matter **11**, 1657 (1999).

[21] S. Greenwald, Acta Crystallogr. **6**, 396 (1953).

[22] K. Tomiyasu, T. Inami, and N. Ikeda, Phys. Rev. B **70**, 184411 (2004).

[23] H. Chen, D. P. Kumah, A. S. Disa, F. J. Walker, C. H. Ahn, and S. Ismail-Beigi, Phys. Rev. Lett. **110**, 186402 (2013).

[24] A. S. Disa, D. P. Kumah, A. Malashevich, H. Chen, D. A. Arena, E. D. Specht, S. Ismail-Beigi, F. J. Walker, and C. H. Ahn, Phys. Rev. Lett. **114**, 026801 (2015).

[25] S. Lee, A. T. Lee, A. B. Georgescu, G. Fabbris, M.-G. Han, Y. Zhu, J. W. Freeland, A. S. Disa, Y. Jia, M. P. M. Dean *et al.*, Phys. Rev. Lett. **123**, 117201 (2019).

[26] P. E. Blöchl, Phys. Rev. B **50**, 17953 (1994).

[27] J. P. Perdew, A. Ruzsinszky, G. I. Csonka, O. A. Vydrov, G. E. Scuseria, L. A. Constantin, X. Zhou, and K. Burke, Phys. Rev. Lett. **100**, 136406 (2008).

[28] G. Kresse and D. Joubert, Phys. Rev. B **59**, 1758 (1999).

[29] D. M. Ceperley and B. J. Alder, Phys. Rev. Lett. **45**, 566 (1980).

[30] J. P. Perdew and A. Zunger, Phys. Rev. B **23**, 5048 (1981).

[31] H. Park, A. J. Millis, and C. A. Marianetti, Phys. Rev. B **92**, 035146 (2015).

[32] J. Chen, A. J. Millis, and C. A. Marianetti, Phys. Rev. B **91**, 241111(R) (2015).

[33] A. A. Mostofi, J. R. Yates, G. Pizzi, Y.-S. Lee, I. Souza, D. Vanderbilt, and N. Marzari, Comput. Phys. Commun. **185**, 2309 (2014).

[34] A. Allred, J. Inorg. Nucl. Chem. **17**, 215 (1961).

[35] L. C. Allen, J. Am. Chem. Soc. **111**, 9003 (1989).

[36] B. R. K. Nanda and S. Satpathy, Phys. Rev. B **79**, 054428 (2009).

[37] L. P. Gor'kov and V. Z. Kresin, Rev. Mod. Phys. **90**, 011001 (2018).

[38] M. B. Salamon and M. Jaime, Rev. Mod. Phys. **73**, 583 (2001).

[39] F. Hellman, A. Hoffmann, Y. Tserkovnyak, G. S. D. Beach, E. E. Fullerton, C. Leighton, A. H. MacDonald, D. C. Ralph, D. A. Arena, H. A. Dürr *et al.*, Rev. Mod. Phys. **89**, 025006 (2017).

[40] E. B. Isaacs and C. A. Marianetti, Phys. Rev. B **94**, 035120 (2016).

[41] E. B. Isaacs and C. A. Marianetti, Phys. Rev. B **95**, 045141 (2017).

[42] J. B. Goodenough, Phys. Rev. **100**, 564 (1955).

[43] J. B. Goodenough, J. Phys. Chem. Solids **6**, 287 (1958).

[44] J. Kanamori, J. Phys. Chem. Solids **10**, 87 (1959).

[45] P. Dutta, M. S. Seehra, S. Thota, and J. Kumar, J. Phys.: Condens. Matter **20**, 015218 (2007).

[46] C. R. Stein, M. T. S. Bezerra, G. H. A. Holanda, J. André-Filho, and P. C. Morais, AIP Adv. **8**, 056303 (2018).

[47] A. Chainani, M. Mathew, and D. D. Sarma, Phys. Rev. B **46**, 9976 (1992).

[48] L. Wang, T. Maxisch, and G. Ceder, Phys. Rev. B **73**, 195107 (2006).

[49] A. T. Lee and M. J. Han, Phys. Rev. B **89**, 115108 (2014).